https://doi.org/10.1016/j.scriptamat.2021.114153

This is the Pre-Published Version.

A novel atomic movement mechanism of intersection-induced bct-α → bcc-α′ martensitic phase transformation

Hui Fu[a], Shuqing Yuan[a], Wanting Sun[a], Jianquan Wan[d], K. C. Chan[a], Jiaming Zhu[c**] and Xu-Sheng Yang[a, b*]

[a]*Advanced Manufacturing Technology Research Centre, Department of Industrial and Systems Engineering, The Hong Kong Polytechnic University, Hung Hom, Kowloon, Hong Kong, China (E-mail: xsyang@polyu.edu.hk)*

[b]*Hong Kong Polytechnic University Shenzhen Research Institute, Shenzhen 518060, China*

[c]*School of Civil Engineering, Shandong University, Jinan 250061, China*

[d]*College of Mechantronics and Control Engineering, Shenzhen University, Shenzhen 518060, China*

The atomic movements for completing the fcc-γ → hcp-ε → bct-α Plastic Deformation-Induced Martensitic Transformation (PDIMT) has been revealed to be confined purely on one specific $\{111\}\gamma$ plane. However, so far nothing has been known for the possible intersection of two fcc-γ → hcp-ε → bct-α PDIMTs pre-developed from two individual $\{111\}\gamma$ slip systems. For the first time, here we capture the nucleation of bcc-α′ in the intersection of two bct-α phases in 304 stainless steel, following a novel polymorphic fcc-γ → hcp-ε → bct-α → bcc-α′ PDIMT. High-resolution transmission electron microscopy observations were mainly performed to unveil the underlying atomic process in the final-step bct-α → bcc-α′ transition, which is executed by the cooperation of partial dislocation dipoles gliding on every second $\{110\}\alpha$ planes of two bct-α phases (equivalent to $\{110\}\alpha'$ and $\{011\}\alpha'$ planes), and atom shuffling along the $[\bar{1}10]\alpha_1/[\bar{1}12]\alpha'$ and $[\bar{1}10]\alpha_2/[21\bar{1}]\alpha'$ directions.

Keywords: Martensitic transformation; Bct and bcc martensites; Stainless steel; Partial dislocation dipole; High-resolution transmission electron microscopy

* Corresponding author. xsyang@polyu.edu.hk (X.-S Yang). Tel: +852-27666604
** Corresponding author. zhujiaming@sdu.edu.cn (J. Zhu).

© 2021. This manuscript version is made available under the CC-BY-NC-ND 4.0 license http://creativecommons.org/licenses/by-nc-nd/4.0/

Martensitic transformation (MT) represents a solid-to-solid diffusionless phase transition with collective movements of atoms less than the nearest interatomic spacing [1]. Specifically, MT accompanied by plastic deformation has been known as the Plastic Deformation-Induced Martensitic Transformation (PDIMT) [2-4], which can cause a cooperative mechanism from transformed hard martensitic particles and soft austenitic matrix (i.e. TRansformation-Induced Plasticity (TRIP) effect) and thus achieve the optimal strength-ductility combination [5-8]. Both body-centered cubic (bcc) α′ and body-centered tetragonal (bct) α martensites can be transited from face-centered cubic (fcc) γ austenite in various metals [9, 10]. For example, the bcc-α′ martensitic phase with lattice constant of $a_{\alpha'}$ = 2.87 Å and bct-α martensitic phase with $a_\alpha = b_\alpha$ (2.94 Å) ≠ c_α (2.55 Å) have been evidenced to transit from the 304 austenitic stainless steels (a_γ = 3.602 Å) [11-13]. More specifically, Fig. 1(a-b) shows the corresponding Bain correspondence, where a 20% compression in the $[001]\gamma$ and 12% expansions in both $[110]\gamma$ and $[\bar{1}10]\gamma$ directions in fcc lattice can transit to a bcc lattice [11]. Whereas, bct lattice can be completed by an 18.4% compression in the $[001]\gamma$ direction (b_α = 2.94 Å) and a 15.3% expansion in the $[110]\gamma$ direction (a_α = 2.94 Å), keeping dimension unchanged in the $[\bar{1}10]\gamma$ direction (c_α = 2.55 Å) [14-16].

Based on the Bain correspondence, several classic hard-sphere shear models have been proposed to describe the atomic movement mechanisms of γ→ α′ PDIMT in steels [17-19]. In 1964, Bogers and Burgers proposed an igneous model with two shear components (i.e. $\frac{a_\gamma}{18}[1\bar{2}\bar{1}]$ slip on each $(11\bar{1})\gamma$ plane and $\frac{a_\gamma}{16}[\bar{1}2\bar{1}]$ slip on each $(111)\gamma$ plane), closing to the average shearing values for forming hexagonal close-packed (hcp) ε martensitic laths. Therefore, Olson and Cohen [20-22] further developed this model for the polymorphic γ→ ε→ α′ PDIMT, hypothesizing the α′ nucleation at the intersection region from two intermediate ε laths. Our

previous works [11, 12] finally provided the atomic-scale evidence for the crucial function from the ε phases and tell-tale transformation features (e.g. the lattice rotation, transition lattices, and excess reverse shear-shuffling), thus for the first time verifying this over 50-year-old Bogers-Burgers-Olson-Cohen (BBOC) model. In addition, γ→ ε→ α′ PDIMT with the α′ nucleation inside single ε lath was also proven to obey the BBOC model in our work [11, 12].

We also discovered and clarified the transition mechanism of another polymorphic γ→ ε→ α PDIMT in austenitic steels, in which α is only nucleated inside single hcp-ε lath [13]. In contrast to γ→ ε→ α′ PDIMTs following BBOC model with two shear components from two $\{111\}\gamma$ planes, atomic movements for the γ→ ε→ α PDIMT, (i.e. Shockley partial dislocations forming intermediate ε, half-Shockley partial dislocation dipoles, and atom shuffling) are all triggered and accomplished purely on one specific $\{111\}\gamma$ plane. It means that two equivalent γ→ ε→ α PDIMTs can occur on two independent $\{111\}\gamma$ systems in austenitic steels. Intersections via shearing and shuffling from two independent $\{111\}\gamma$ systems can happen frequently in low-stacking fault energy (SFE) metals, such as twin-twin intersection [23], polymorphic γ→ twin→ α′ [24] and γ→ ε → α′ PDIMTs [12]. However, so far no literature has been reported regarding the intersection from two γ→ ε→ α PDIMTs, which might be due to the complex and key transition signatures from two polymorphic PDIMTs that are difficult to detect and analyze.

By conducting high-resolution transmission electron microscope (HRTEM) observations, herein, for the first time we have captured the nucleation of bcc-α′ in the intersection of two γ→ ε→ α PDIMTs in AISI 304 austenitic stainless steel by the surface mechanical attrition treatment (SMAT), thus discovering a novel polymorphic fcc-γ → hcp-ε → bct-α → bcc-α′ PDIMT. The composition of the 304 stainless steel specimen and SMAT parameters were described in Refs. [11-13]. The SMAT process causes a plastic strain field that

is extremely severe in the surface and then gradually decreased towards to the center of the specimen. The polymorphic γ→ ε→ α PDIMT was revealed to occur in the top surface of the SMATed specimen and corresponding atomic movement mechanisms were uncovered successfully by dissecting the microstructure evolution along the cross sectional direction [13]. In the present work, atomic-level HRTEM observations were therefore carefully conducted in the top surface of the SMATed specimen to capture and unveil the atomic process in the final transition step with bct-α→ bcc-α′. HRTEM observations in the top surface layer were performed using a field emission JEM-2100F TEM operated at a voltage of 200 kV. TEM samples were firstly mechanically polished to ~15 μm from the side away from the topmost surface. After that, the TEM foils were further thinned by the precision ion polishing system Gatan 691 before the TEM observations.

Fig. 1(c) gives a typical bright-field (BF) TEM image in the top surface in SMATed 304 stainless steel, exhibiting profuse intersections from crossed laths in this region. The TEM image in Fig. 1(d) and corresponding HRTEM image in Fig. 1(e) are enlarged from the white square in Fig. 1(c), clearly showing that the bcc-α′ martensitic inclusion is nucleated at the intersection site from two bct-α intermediate phases pre-formed via fcc-γ→ hcp-ε→ bct-α PDIMTs. Once nucleated, the bcc-α′ inclusion tends to further grow into the γ matrix, leading to its width larger than that of bct-α phases and hcp-ε laths, as shown in Fig. 1(e). The inset in Fig. 1(e) is the associated fast Fourier transformation (FFT) pattern of the inclusion α′ and surrounding phases (i.e. γ and α). Accordingly, Fig. 1(f) schematically summarizes the orientation relationships (ORs) based on the FFT pattern, indicating that the α′ inclusion exhibits the Pitsch OR ($[\bar{1}10]\gamma // [1\bar{1}1]\alpha'$, $(00\bar{2})\gamma // (10\bar{1})\alpha'$) with respect to γ, which is different from the ORs between two adjacent α phases and matrix γ, i.e. Nishiyama-Wassermann (N-W)1 OR ($[\bar{1}10]\gamma // [00\bar{1}]\alpha_1$, $(111)\gamma//(110)\alpha_1$) and N-W2 OR ($[\bar{1}10]\gamma // [[00\bar{1}]\alpha_2$, $(11\bar{1})\gamma//(110)\alpha_2$) [19, 25]. The N-W OR keeps the closest packing {111}γ planes

unrotated from (111)γ to (110)α during the fcc-γ→ bct-α PDIMTs [13]. However, when α′ inclusion nucleates and grows by the intersection of two α phases, these two closest packing {111}γ planes are both rotated to form the Pitsch OR in the intersection site, which is in the middle of two N-W ORs. The misorientation between the Pitsch OR and either of the two N-W ORs is 5.26°. Previous studies have reported the one-step fcc-γ → bcc-α′ [26], polymorphic fcc-γ→ hcp-ε→ bcc-α′ [11, 12] and polymorphic fcc-γ→ hcp-ε→ bct-α [13] PDMITs, in which hcp-ε phase is the intermediate phase. The novel polymorphic fcc-γ→ hcp-ε→ bct-α→ bcc-α′ PDIMT discovered in the present work interestingly indicate that both hcp-ε and bct-α martensitic phases can serve as the intermediate phases for the transition of bcc-α′ martensite. It also can explain why high-density bcc-α′ phase (instead of bct-α) was normally observed in steels during plastic deformation [27-30]. In the following sections, we will focus on the transition mechanism of final step with bct-α→ bcc-α′.

To explore the atomic movement mechanisms in the α→α′ transition, HRTEM observations are mainly focused on the interface structures between the α′ inclusion and adjacent α and γ phases, as a typical HRTEM image captured in Fig. 2(a). More specifically, Fig. 2(b-g) give the detailed enlarged Fourier-filtered images and corresponding atomic spacings of the α_1/α', α_2/α' and γ/α' interfaces, respectively. There are four noticeable characteristics drawn in these interface structures. Firstly, when the intersection action between α_1 and α_2 phases is cooperatively completed to form the α′ phase, it is directly evidenced that both $(110)\alpha_1$ and $(110)\alpha_2$ planes are rotated +5.26° and -5.26° respectively to become the (110)α′ and (011)α′ planes, as the HRTEM image marked in Fig. (a). It changes the angle between $(110)\alpha_1$ and $(110)\alpha_2$ (corresponding to $(111)\gamma$ and $(11\bar{1})\gamma$ planes), decreasing from the original 70.52° to 60° between (110)α′ and (011)α′ in bcc-α′ phase. Accordingly, two N-W ORs in α_1 and α_2 phase are transited to the Pitsch OR in α′ phase in the intersection site, which is consistent with the ORs summarized in Fig. 1(f). Secondly, the typical diffuse interfacial

structures are observed for α_1/α' interface (i.e. between the $(1\bar{1}0)\alpha_1$ and $(\bar{1}12)\alpha'$ planes) and α_2/α' interface (i.e. between the $(1\bar{1}0)\alpha_2$ and $(21\bar{1})\alpha'$ planes), respectively, as shown in Fig. 2(b) and (d). Fig. 2(b) and (d) demonstrates that the angles of $(1\bar{1}0)\alpha_1$ plane to $[1\bar{1}0]\alpha_1$ direction in the α_1 phase and $(1\bar{1}0)\alpha_2$ plane to $[1\bar{1}0]\alpha_2$ direction in the α_2 phase are both 90°, correspondingly, which transit to inclined 60° of $(011)\alpha'$ plane to $[\bar{1}12]\alpha'$ direction and $(110)\alpha'$ plane to $[21\bar{1}]\alpha'$ direction in the bcc-α' phase. Different from that in Fig. 2(d), it is noted that there is such obvious rotation of 5.26° in $(110)\alpha_1$ plane within the diffuse interfacial region in Fig. 2(b), which could be further accomplished via dislocation walls or continuous lattice deformation inside α' inclusion [11, 12]. Thirdly, the atomic spacing along the $[1\bar{1}0]\alpha_1$ direction and $[1\bar{1}0]\alpha_2$ is $d_{[1\bar{1}0]\alpha 1} = d_{[1\bar{1}0]\alpha 2} = 2.08$ Å, smaller than that of corresponding to final $[\bar{1}12]\alpha'$ and $[21\bar{1}]\alpha'$ directions ($d_{[\bar{1}12]\alpha'} = d_{[21\bar{1}]\alpha'} = 2.34$ Å) as shown in Fig. 2(e) and Fig. 2(f), respectively. However, the atomic planar spacing of $\{110\}\alpha$ and $\{110\}\alpha'$ are equivalent to be 2.08 Å. Lastly, the α' phase shows a Pitsch OR with respect to the γ phase as shown in Fig. 2(g). Clearly, the γ/α' interface is semi-coherent diffuse interface having two sets of misfit dislocations can be determined as $\boldsymbol{b}_\gamma^{\boldsymbol{I}} = a/2[01\bar{1}]$ (marked by white arrow) on $(111)\gamma$ and $\boldsymbol{b}_\gamma^{\boldsymbol{II}} = \alpha/2[0\bar{1}\bar{1}]$ (marked by yellow arrow) on $(11\bar{1})\gamma$ planes, which have the same component of their Burgers vectors, $b_{[00\bar{1}]} = 1.80$ Å, along the $[00\bar{1}]\gamma$ direction. Note that a lattice misfit strain (i.e. $f = 10.95\%$) is existed between the $(00\bar{2})\gamma$ and $(10\bar{1})\alpha'$ planes. Accordingly, the misfit dislocation array with the spacing, $l_d = b_{[00\bar{1}]}/f = 16.5$ Å, which is approximately equivalent to the total interplanar spacing of either 8 $(10\bar{1})\alpha'$ or 9 $(00\bar{2})\gamma$ planes as shown in Fig. 2(g), These misfit dislocation arrays should be distributed to release the above lattice misfit strain.

The above analysis signifies that the final-step transition from bct-α to bcc-α′ is accomplished by simultaneously decreasing both angles of $(1\bar{1}0)\alpha_1$ plane to $[1\bar{1}0]\alpha_1$ direction, $(1\bar{1}0)\alpha_2$ plane to $[1\bar{1}0]\alpha_2$ direction and increasing the atomic spacing along the $[1\bar{1}0]\alpha_1$ / $[\bar{1}12]\alpha'$ and $[1\bar{1}0]\alpha_2$ / $[21\bar{1}]\alpha'$ directions. Accordingly, our atomic-level characterizations further successfully illustrate the detailed atomic process for the completion of these two transition actions. On one hand, as indicated in Fig. 2(b) and Fig. 2(d), two arrays of partial dislocation dipoles, $\boldsymbol{b_p}$: $\boldsymbol{-b_p}$, can be indexed within the α_1/α' and the α_2/α' interfacial regions. Dislocation dipoles are pairs of parallel dislocations with opposite sign of Burgers vectors. More specifically, the partial dislocations dipoles in Fig. 2(c) shows that one partial, $\boldsymbol{b_p}$, glides on one side of a $(110)\alpha_1/(110)\alpha'$ plane, while the partner of $\boldsymbol{-b_p}$, glides on the other side of the same $(110)\alpha_1/(110)\alpha'$ plane. Therefore, slipping this dislocation dipoles in "sandwich" manner can flexibly switch the angles, decreasing the angles of $(1\bar{1}0)\alpha_1$ plane to $[1\bar{1}0]\alpha_1$ and $(1\bar{1}0)\alpha_2$ plane to $[1\bar{1}0]\alpha_2$ from original 90° to corresponding angle of near 60° in α′ phase, as shown in Fig. 2(b-d) and in Fig. 2(e-f). It should also be noticed that slipping the dislocation dipoles with opposite signs in pairs does not result in the macro-scale shearing strain because of the net zero Burgers vector, which indicates that the required energy for the martensitic transformation can be significantly lowered [31, 33]. The partial dislocation dipoles have been widely reported in various metals, such as Cu [32], Mg [33] and TiAl alloy [34], etc. If taking α' phase as a reference, the displacement of each partial dislocation is equal to the half of atomic spacing along $[\bar{1}12]\alpha'$ or $[21\bar{1}]\alpha'$ directions in α′ phase. The determination of the Burgers vectors of two sets of partial dislocation dipoles on $(110)\alpha_1/(110)\alpha'$ planes in the α_1/α' and $(110)\alpha_2/(011)\alpha'$ planes in the α_2/α' interfacial regions will be elucidated in the following sections. On the other hand, the evolutions of the atomic spacing along the $[1\bar{1}0]\alpha_1/[\bar{1}12]\alpha'$ and $[1\bar{1}0]\alpha_2/[21\bar{1}]\alpha'$ directions in the diffuse α_1/α' and the α_2/α' interfaces are measured and given in Fig. 2(e) and

Fig. 2(f), respectively, indicating that the atomic spacing is gradually increased from the original 2.08 Å in two α phases to 2.34 Å along $[\bar{1}12]\alpha'$ and $[21\bar{1}]\alpha'$ directions in α′ phase. This process is apparently completed by atom shuffling, as reported by previous works [13]. In addition, the geometric phase analysis (GPA) method was employed to obtain the strain maps for understanding the localized strain in the interfacial regions [35]. Taking α′ as the reference lattice, Fig. 2(h-i) shows the distributions of in-plane strain (E_{xx}) and out-plane strain (E_{yy}) in the α′/α_1, α′/α_2 and α′/γ interfacial regions, respectively. Accordingly, the averaged strain profiles (E_{xx} and E_{yy}) scanned along the diffuse interfacial regions are also quantitatively given in Fig. 2(j). Followed by the slight incensement initially, E_{xx} and E_{yy} are maintained at relatively low levels in α′/α_1 and α′/α_2 interfaces, in which only a fluctuation of E_{xx} exists, without significant accumulation caused by the atomic collective movement. This might be due to the relaxation of the strain/stress fields caused by the zero-strain partial dislocation dipoles slipping for switching the incline angles and localized atom shuffling for gradually expanding the atomic spacing in the interfacial regions. Based on above analysis, our atomic characterizations reveal that the slipping of partial dislocations dipoles and atom shuffling are cooperative to accomplish the final-step α→α′ transition with the rotation of the OR from two N-W ORs to Pitsch OR.

Since bcc structure has the higher symmetry than that of bct structure, the bcc structure is taken as a reference to describe the dislocation system in our work. Our atomic characterizations of the diffusion α/α′ interfaces and the particular dislocations system in the crystalline structure of bcc-α′ can be incorporated to determine the Burgers vectors of the dislocation dipoles in Fig. 2(b) and (d). The slip of $a/2[\bar{1}11]$ on (110)α′ plane with the shortest lattice vector represents a perfect dislocation in bcc structure [36]. Fig. 3(a) shows a most commonly (110)α′ close-packed plane with an ABABAB stacking sequence. Note that three {110}α′ type planes intersect along one specific <111>α′ direction. Therefore, screw

dislocations with wavy and ill-defined slip lines can be generated to move in any of the three {110} planes. Similar to the fcc structure, Fig. 3(a) shows that in moving the B-layer along $[\bar{1}11]\alpha'$ direction can be realized by successively shearing three partial dislocations indicated by $\boldsymbol{b_1}$, $\boldsymbol{b_2}$ and $\boldsymbol{b_3}$. In other words, a possible dissociation reaction in bcc structure can be expressed as [37]: $a/2[\bar{1}11] \rightarrow a/8[\bar{1}10] + a/4[\bar{1}12] + a/8[\bar{1}10]$. It indicates that the partial dislocations have respectively Burges vectors of $\boldsymbol{b}_{p1}$=$\boldsymbol{b}_{p3} = a/8[\bar{1}10]$ and $\boldsymbol{b}_{p2}$= $a/4[\bar{1}12]$ on (110)α′ plane. Similarly, the possible dissociation reaction for the screw dislocation a/2$[11\bar{1}]$ on (011)α′ plane should be expressed as: $a/2[11\bar{1}] \rightarrow a/8[01\bar{1}] + a/4[21\bar{1}] + a/8[01\bar{1}]$, where partial dislocations have Burges vectors of $\boldsymbol{b}_{p1}$= $\boldsymbol{b}_{p3}$= $a/8[01\bar{1}]$ and $\boldsymbol{b}_{p2}$= $a/4[21\bar{1}]$ on (011)α′ plane, respectively. Clearly, gliding dislocations either along $\boldsymbol{b}_{p1}$/$\boldsymbol{b}_{p3}$ or $\boldsymbol{b}_{p2}$ directions on (110)α′ planes can decrease the angles of $(1\bar{1}0)\alpha_1$ plane to $[1\bar{1}0]\alpha_1$ and $(1\bar{1}0)\alpha_2$ plane to $[1\bar{1}0]\alpha_2$, as shown in Fig. 3(b), where $\boldsymbol{b}_{p1}$/$\boldsymbol{b}_{p3}$ and $\boldsymbol{b}_{p2}$ have different inclined angles with respect to the dislocation lines of $[1\bar{1}1]\alpha'$. Accordingly, two types of partial dislocation dipoles, i.e. $a/6[\bar{1}12] : -a/6[\bar{1}12]$ (2/3$\boldsymbol{b}_{p2}$: -2/3$\boldsymbol{b}_{p2}$) and $9a/16[\bar{1}10] : -9a/16[\bar{1}10]$ (9/2$\boldsymbol{b}_{p1}$/$\boldsymbol{b}_{p3}$: -9/2$\boldsymbol{b}_{p1}$/$\boldsymbol{b}_{p3}$), can be proposed to completely decrease the angles of $(1\bar{1}0)\alpha$ planes to $[1\bar{1}0]\alpha$ directions, from 90° to near 60° in α′ phase. However, it should be noted that the gliding the dislocation dipoles $9a/16[\bar{1}10] : -9a/16[\bar{1}10]$ (9/2$\boldsymbol{b}_{p1}$/$\boldsymbol{b}_{p3}$: -9/2$\boldsymbol{b}_{p1}$/$\boldsymbol{b}_{p3}$) with larger Burgers vectors is obviously less energetic favored, since the strain energy of dislocation is proportional to Gb^2 [37]. Therefore, two arrays of $\boldsymbol{b}_p$: -$\boldsymbol{b}_p$ partial dislocation dipoles, 2/3$\boldsymbol{b}_{p2}$: -2/3$\boldsymbol{b}_{p2}$, are confirmed in the current case. In addition, the atomic displacement along the $[00\bar{1}]\alpha_1$ and $[00\bar{1}]\alpha_2$ directions induced by these partial dislocation dipoles should be none since $[00\bar{1}]\alpha_1 // [00\bar{1}]\alpha_2 // [1\bar{1}1]\alpha'$.

Fig. 3(c-e) illustrates schematically the lattice evolution from bct-α to bcc-α′ lattice under the projection along the $[\bar{1}10]\gamma //[00\bar{1}]\alpha_1 //[00\bar{1}]\alpha_2 //[1\bar{1}1]\alpha'$ directions, elucidating the cooperation function of partial dislocation dipoles and atom shuffle. More specifically, as shown in Fig. 3c, the angle between (110)α_1 and (110)α_2 is 70.52° due to the N-W ORs between α_1, α_2 and γ phases. Two arrays of partial dislocation dipoles $\boldsymbol{b_p}$:-$\boldsymbol{b_p}$, i.e. $a/6[\bar{1}12]:-a/6[\bar{1}12]$ and $a/6[21\bar{1}]:-a/6[21\bar{1}]$ glide along two sides of every (110)α_1/(110)α′ planes and (110)α_2/(011)α′, respectively. Cooperatively gliding these partial dislocation dipoles in "sandwich" manner can switch the angles of $(1\bar{1}0)\alpha_1$ plane to $[1\bar{1}0]\alpha_1$ and $(1\bar{1}0)\alpha_2$ plane to $[1\bar{1}0]\alpha_2$ at the intersection site, decreasing from the original 90° to near 60°, as shown in Fig. 3(d). The left angle deviation can be adjusted during the synchronically and cooperatively atom shuffling process, which also expands the atomic spacing along the $[1\bar{1}0]\alpha_1/[\bar{1}12]\alpha'$ and $[1\bar{1}0]\alpha_2/[21\bar{1}]\alpha'$, increasing from the original $d_{[1\bar{1}0]\alpha 1}=d_{[1\bar{1}0]\alpha 2}$ =2.08 Å in two α phases to final $d_{[\bar{1}12]\alpha'}=d_{[21\bar{1}]\alpha'}$ =2.34 Å in α' phase, as shown in Fig. 3(e). It should be pointed out that if atomic spacing along the $[1\bar{1}0]\alpha_1/[\bar{1}12]\alpha'$ direction is individually expanded by atom shuffling to 2.34 Å, the atomic spacing along $[1\bar{1}0]\alpha_2/[21\bar{1}]\alpha'$ will automatically beyond 2.34 Å, and vice versa. Therefore, the nucleation of the bcc-α′ phase in the α→α′ transition should be completed through the cooperation of partial dislocation dipoles gliding and atom shuffling from two intersectional α_1 and α_2 phases, denoting a Pitsch OR between α' the γ phases.

The Bain correspondence between the bct-α and bcc-α′ lattices for the final-step transition with α→α′ is schematically depicted in Fig. 4(a). The lattice constants, $a_\alpha = b_\alpha = 2.94$ Å, $c_\alpha = 2.55$ Å, in the present work are equivalent to that in the previous work [13]. Two partial dislocations, i.e. $a/6[\bar{1}12]$ on (110)α′ plane and $a/6[21\bar{1}]$ on (011)α′ plane, are labeled in

Fig. 4(a), which provide two arrays of $\boldsymbol{b_p}$: $\boldsymbol{-b_p}$ partial dislocation dipoles, i.e. $a/6[\bar{1}12]$: $-a/6[\bar{1}12]$ on (110) α′ and $a/6[21\bar{1}]:-a/6[21\bar{1}]$ on (011)α′ planes, respectively. As a result, the cooperative action of the two arrays of partial dislocation dipoles and atom shuffling decrease the inclined angles of $(1\bar{1}0)\alpha$ planes to $[1\bar{1}0]\alpha$ directions and generate a tension along $[1\bar{1}0]\alpha_1/[\bar{1}12]\alpha'$ and $[1\bar{1}0]\alpha_2/[21\bar{1}]\alpha'$ directions in the two α phases, as schematically shown in Fig. 4(b), denoting the lattice constants of $a_{\alpha'}= b_{\alpha'}= c_{\alpha'}= 2.87$ Å in the transited bcc-α′ lattice. Fig. 4(c-d) schematically summarizes and compares the atomic movement mechanisms of the polymorphic fcc-γ→ hcp-ε→ bct-α and fcc-γ→ hcp-ε→ bct-α→bcc-α′ PDIMTs. Our previous work has revealed that the fcc-γ→ hcp-ε→ bct-α transition is accomplished by cooperation of half-Shockley partial dislocation dipoles and atom shuffling, with all atomic movements purely on one specific {111}γ//{0001}ε planes. When the intersection action is from two fcc-γ→ hcp-ε→ bct-α PDIMTs on two independent {111}γ//{0001}ε planes, the nucleation of the bcc-α′ inclusion in the intersection site indicates a new polymorphic fcc-γ→ hcp-ε→ bct-α→bcc-α′ PDIMT. Noticeably, the partial dislocation dipoles and atom shuffling that simultaneously take place from two bct-α intermediate phases would cooperatively accomplish the final-step transition from bct-α to bcc-α′ in the present work. On one hand, slipping low-energy partial dislocation dipoles can flexibly convert the stacking sequence of the mobile phase interface [32-34], which can lead to unstable stacking fault and relieve the internal stress/strain field within the diffuse interfaces. On the other hand, the unstable stacking fault energy and associated low energy status could be beneficial to the atoms shuffle themselves for tailoring the atomic spacing [38, 39]. As a result, the combination of the slipping of partial dislocations dipoles and atom shuffling play a pivotal role in accomplishing the polymorphic PDIMTs, such as the fcc-γ→ hcp-ε→ bct-α→bcc-α′ PDIMT in the current work. The novel findings in this study further shed light on the atomic

mechanisms of the PDIMTs in steels and stimulate innovative ideas to understand other solid-to-solid phase transition.

This work was supported by the National Natural Science Foundation of China Projects (Nos. 51701171 and 51971187) and the PolyU Postdoctoral Fellowships Scheme (No. G-YW5N). SY was supported by the grant from the PolyU Research Committee under student account code RK2J.

References

1. C.S. Smith, A History of Metallography: The Development of Ideas on the Structure of Metals Before 1890, Cambrige, Massachusetts London, 2012.
2. X.L. Wu, M.X. Yang, F.P. Yuan, L. Chen, Y.T. Zhu, Acta Mater. 112 (2016) 337-346.
3. Y. Tomita, T. Iwamoto, Int. J. Mech. Sci. 37 (12) (1995) 1295-1305.
4. J. Liu, Y. Jin, X. Fang, C. Chen, Q. Feng, X. Liu, Y. Chen, T. Suo, F. Zhao, T. Huang, H. Wang, X. Wang, Y. Fang, Y. Wei, L. Meng, J. Lu, and W. Yang, Sci. Rep. 6 (2016) 35345.
5. S.-H. Kim, H. Kim, N.J. Kim, Nature 518 (7537) (2015) 77-79.
6. Z. Li, K.G. Pradeep, Y. Deng, D. Raabe, C.C. Tasan, Nature 534 (7606) (2016) 227-230.
7. S. Jiang, H. Wang, Y. Wu, X. Liu, H. Chen, M. Yao, B. Gault, D. Ponge, D. Raabe, A. Hirata, M. Chen, Y. Wang, and Z. Lu, Nature 544 (7651) (2017) 460-464.
8. B.B. He, B. Hu, H.W. Yen, G.J. Cheng, Z.K. Wang, H.W. Luo, M.X. Huang, Science 357 (2017) 1029-1032.
9. D. Ma, M. Yao, K.G. Pradeep, C.C. Tasan, H. Springer, D. Raabe, Acta Mater. 98 (2015) 288-296.
10. A. Shibata, H. Yonezawa, K. Yabuuchi, S. Morito, T. Furuhara, T. Maki, Mater. Sci. Eng. A 438-440 (2006) 241-245.
11. X.S. Yang, S. Sun, X.L. Wu, E. Ma, T.Y. Zhang, Sci. Rep. 4 (2014) 6141.
12. X.-S. Yang, S. Sun, T.-Y. Zhang, Acta Mater. 95 (2015) 264-273.
13. X.-S. Yang, S. Sun, H.-H. Ruan, S.-Q. Shi, T.-Y. Zhang, Acta Mater. 136 (2017) 347-354.
14. H. Zheng, A. Cao, C.R. Weinberger, J.Y. Huang, K. Du, J. Wang, Y. Ma, Y. Xia, S.X. Mao, Nat. Commun. 1 (9) (2010) 144.
15. J. Diao, K. Gall, M.L. Dunn, Nat. Mater. 2 (10) (2003) 656-660.
16. J. Diao, K. Gall, M.L. Dunn, Phys. Rev. B 70 (7) (2004) 075413.
17. G. Kurdjumov, G. Sachs, Zeit. F. Phys. 64 (1930) 325-343.
18. A.J. Bogers, W.G. Burgers, Acta Metall. 12 (2) (1964) 255-261.
19. Z. Nishiyama, Sci. Rep. Tohoku Univ. 23 (1934) 637-664.
20. G. Olson, M. Cohen, J. Less Common Met. 28 (1) (1972) 107-118.
21. G. Olson, M. Cohen, Metall. Trans. A 7 (12) (1976) 1905-1914.
22. G. Olson, M. Cohen, Annu. Rev. Mater. Sci. 11 (1) (1981) 1-32.
23. S. Zhao, Q. Zhu, K. Song, H. Zhou, J. Wang, Scripta Mater. 188 (2020) 184-189.

24. A.Y. Chen, H.H. Ruan, J. Wang, H.L. Chan, Q. Wang, Q. Li, J. Lu, Acta Mater. 59 (9) (2011) 3697-3709.
25. G. Wasserman, Eisenhuttenwea 16 (1933) 647.
26. Y. Gao, Y. Wang, Phys. Rev. Mater. 2 (9) (2018) 093611.
27. L. Bracke, L. Kestens, J. Penning, Scripta Mater. 57 (5) (2007) 385-388.
28. A.Y. Chen, H.H. Ruan, J.B. Zhang, X.R. Liu, J. Lu, Mater. Chem. Phys. 129 (3) (2011) 1096-1103.
29. K.S. Mao, C. Sun, C.-H. Shiau, K.H. Yano, P.D. Freyer, A.A. El-Azab, F.A. Garner, A. French, L. Shao, J.P. Wharry, Scripta Mater. 178 (2020) 1-6.
30. T. Wang, J. Du, S. Wei, F. Liu, Prog. Nat. Sci. Mater. 31 (1) (2021) 121-128.
31. A.S. Tetelman, Acta Metall. 10 (9) (1962) 813-820.
32. M.E. Kassner, M.T. Pérez-Prado, K.S. Vecchio, M.A. Wall, Acta Mater. 48 (17) (2000) 4247-4254.
33. X. Liu, J. Wang, Sci. Rep. 6 (1) (2016) 21393.
34. Y. He, Z. Liu, G. Zhou, H. Wang, C. Bai, D. Rodney, F. Appel, D. Xu, R. Yang, Scripta Mater. 143 (2018) 98-102.
35. M.J. Hÿtch, E. Snoeck, R. Kilaas, Ultrami croscopy 74 (3) (1998) 131-146.
36. G.M. Cheng, W.Z. Xu, W.W. Jian, H. Yuan, M.H. Tsai, Y.T. Zhu, Y.F. Zhang, P.C. Millett, J Mater. Res. 28 (13) (2013) 1820-1826.
37. R.E. Smallman, A.H.W. Ngan, Introduction to Dislocations, in Modern Physical Metallurgy, 2014, pp. 121-158.
38. B. Li, E. Ma, Phys. Rev. Lett. 103 (3) (2009) 035503.
39. H. El Kadiri, C.D. Barrett, M.A. Tschopp, Acta Mater. 61 (20) (2013) 7646-7659.

Figure 1

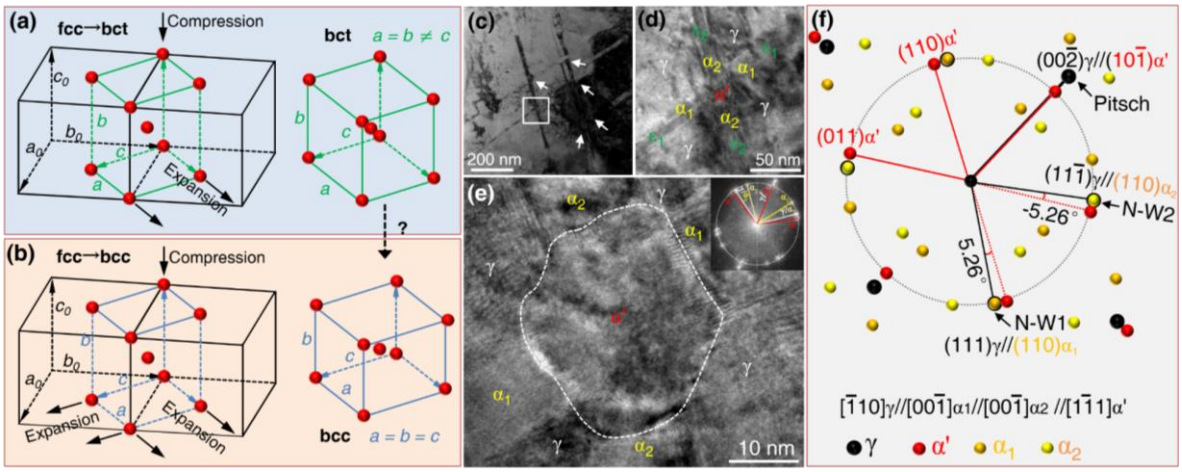

Fig. 1. The α (bct)→α′ (bcc) transformation. Schematic of martensitic transition of (a) fcc→ bct and (b) fcc→ bcc transformation on the basis of the Bain path. (c) Typical BF TEM image taken in the top surface layer of SMATed 304 stainless steel. High density of bcc-α′ martensitic inclusions (white arrows) are formed at the intersection region of crossed lath phases. Enlarged TEM (d) and HRTEM (e) images show the bcc-α′ martensitic inclusion formed from two intersected bct-α phases, the inset in (e) is the corresponding FFT pattern of the inclusion and surrounding phases. (f) Schematic summarizing the diffraction spots from (e) for the ORs between the γ, α_1, α_2 and α′.

Figure 2

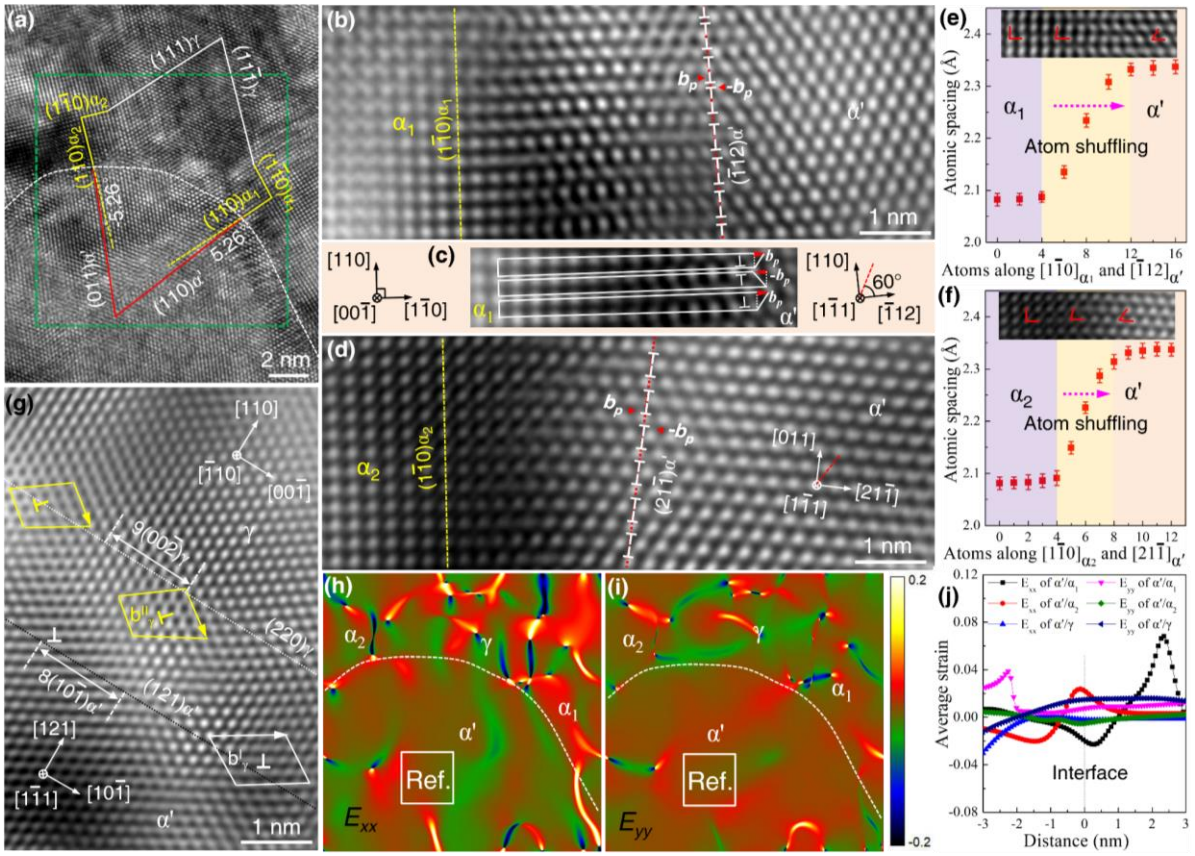

Fig. 2. Interfacial structures between α′ inclusion and adjacent α and γ phases. (a) HRTEM image of the γ/α/α′ interface. The corresponding Fourier filtered images of the (b) α_1/α' interface, (d) α_2/α' interface and (g) γ/α′ interface, respectively. (c) The detailed Burgers circuit for indexing the partial dislocation dipoles, $\boldsymbol{b_p}$: $\boldsymbol{-b_p}$, in the α_1/α' interfacial region. (e) The measurement of atomic spacing at several representative atomic positions along the $[\bar{1}12]\alpha'$ direction from α_1 to α′ in the α_1/α' diffuse interface region of (b). (f) The measurement of atomic spacing at several representative atomic positions along the $[21\bar{1}]\alpha'$ direction from α_2 to α′ in the α_2/α' diffuse interface region of (d). The insets show inclined angles of $(1\bar{1}0)\alpha_1$ plane to $[1\bar{1}0]\alpha_1$ direction and $(1\bar{1}0)\alpha_2$ plane to $[1\bar{1}0]\alpha_2$ direction, from 90° to corresponding inclined angle of 60° in α′ phase. 2D E_{xx} (h) and E_{yy} maps (i) of α'/α_1,α'/α_2 and α′/γ, respectively, taken from the green dash square region in (a). (j) Averaged strains (E_{xx} and E_{yy}) in α'/α_1,α'/α_2 and α′/γ interfaces.

Figure 3

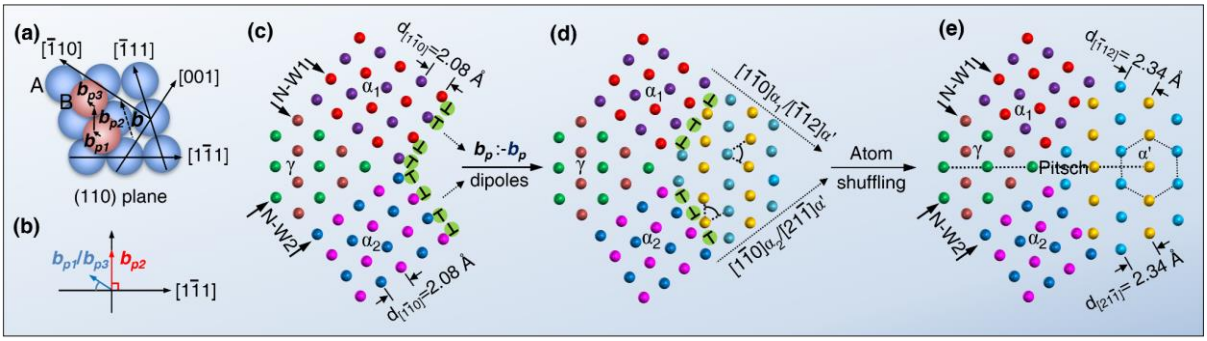

Fig. 3. **The transition mechanism of α→ α′**. (a) Schematic of the (110) plane of the bcc lattice. blue atoms represent A layer while red atoms represent B layer. Three types of partial dislocations have different inclined angle with respect to the dislocation lines of $[1\,\bar{1}1]\alpha'$. (c)-(e) Schematic diagrams for the cooperative role of partial dislocation dipoles and atom shuffling in the lattice evolutions from α to α′.

Figure 4

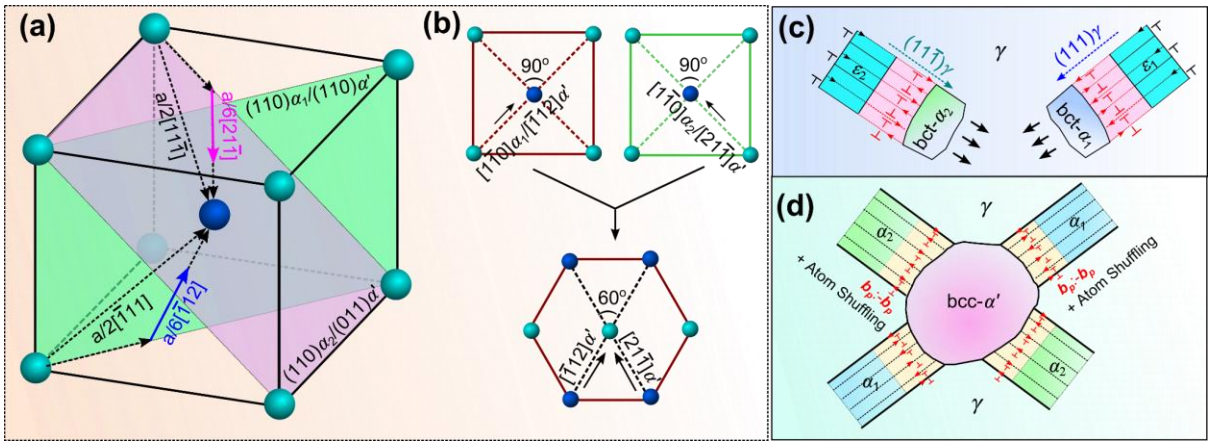

Fig. 4. **The schematic diagram of polymorphic fcc-γ → hcp-ε→ bct-α→ bcc-α′ PDIMT**. (a) The Bain correspondence between the original bct-α and the final bcc-α′ for the transition α→α′. (b) Projected along $[00\bar{1}]\alpha$ //$[1\bar{1}1]\alpha'$ directions, the concurrent decrease of the angle of $(1\bar{1}0)\alpha$ plane to $[1\bar{1}0]\alpha$ and an expansion along $[1\bar{1}0]\alpha_1/[\bar{1}12]\alpha'$ and $[1\bar{1}0]\alpha_2/[21\bar{1}]\alpha'$ transits the α lattice to the α′ lattice. (c) Schematic summarizing of atomic movement mechanisms of the polymorphic fcc-γ→ hcp-ε→ bct-α and (d) intersection-induced fcc-γ→ hcp-ε→ bct-α→bcc-α′ PDIMTs.